



## Wireless, battery-free, remote photoactivation of caged-morphine for photopharmacological pain modulation without side effects

Minsung Kim<sup>a,b,1</sup>, Marc López-Cano<sup>c,d,1</sup>, Kaiqing Zhang<sup>e,f,1</sup>,  
 Yue Wang<sup>a,g,1</sup>, Xavier Gómez-Santacana<sup>h</sup>, África Flores<sup>c,d</sup>,  
 Mingzheng Wu<sup>a,i</sup>, Shupeng Li<sup>e</sup>, Haohui Zhang<sup>e</sup>,  
 Yuanting Wei<sup>e</sup>, Xiuyuan Li<sup>e,j</sup>, Cameron H. Good<sup>a,b,k</sup>,  
 Anthony R. Banks<sup>a,b,k</sup>, Amadeu Llebaria<sup>g</sup>, Jordi Hernando<sup>l</sup>,  
 Sung-Hyuk Sunwoo<sup>m</sup>, Jianyu Gu<sup>a</sup>, Yonggang Huang<sup>a,e,n,o,\*</sup>,  
 Francisco Ciruela<sup>c,d,\*\*</sup>, John A. Rogers<sup>a,g,k,n,o,p,\*\*\*</sup>

<sup>a</sup> Querrey Simpson Institute for Bioelectronics, Northwestern University, Evanston, IL, 60208, USA

<sup>b</sup> Neurolux Inc., Northfield, IL, 60093, USA

<sup>c</sup> Pharmacology Unit, Department of Pathology and Experimental Therapeutics, Faculty of Medicine and Health Sciences, Institute of Neurosciences, University of Barcelona, L'Hospitalet de Llobregat, 08907, Spain

<sup>d</sup> Neuropharmacology and Pain Group, Neuroscience Program, Bellvitge Biomedical Research Institute, L'Hospitalet de Llobregat, 08907, Spain

<sup>e</sup> Department of Civil and Environmental Engineering, Northwestern University, Evanston, IL, 60208, USA

<sup>f</sup> State Key Laboratory of Structural Analysis, Optimization and CAE Software for Industrial Equipment, Department of Engineering Mechanics, Dalian University of Technology, Dalian, Liaoning, 116024, China

<sup>g</sup> Department of Biomedical Engineering, Northwestern University, Evanston, IL, 60208, USA

<sup>h</sup> MCS - Medicinal Chemistry & Synthesis, Institute for Advanced Chemistry of Catalonia (IQAC-CSIC), Barcelona, Spain

<sup>i</sup> Department of Neurobiology, Northwestern University, Evanston, IL, 60208, USA

<sup>j</sup> State Key Laboratory of Mechanical System and Vibration, School of Mechanical Engineering, Shanghai Jiao Tong University, Shanghai, 200240, China

<sup>k</sup> Center for Bio-Integrated Electronics, Northwestern University, Evanston, IL, 60208, USA

<sup>l</sup> Departament de Química, Universitat Autònoma de Barcelona, Edifici C/n, Campus UAB, Cerdanyola del Vallès, 08193, Spain

<sup>m</sup> Department of Chemical Engineering, Kumoh National Institute of Technology, Gumi, 39177, Republic of Korea

<sup>n</sup> Department of Mechanical Engineering, Northwestern University, Evanston, IL, 60208, USA

<sup>o</sup> Department of Materials Science and Engineering, Northwestern University, Evanston, IL, 60208, USA

<sup>p</sup> Department of Neurological Surgery, Feinberg School of Medicine, Northwestern University, Chicago, IL, 60611, USA

### ARTICLE INFO

#### Keywords:

Implantable wireless devices  
 Battery-free optical systems  
 Photopharmacology  
 Caged morphine  
 Pain modulation  
 Opioid side effect reduction

### ABSTRACT

Chronic pain severely impairs physical, psychological, and cognitive functions. While opioid-based therapies can be effective, they are limited by tolerance, dependence, and adverse side effects, highlighting the need for safer alternatives. Recent advances in photopharmacology allow precise modulation of pain-related neuronal circuits, offering improved control and effectiveness. For delivery of light, fully implantable, wireless, battery-free optical systems in miniaturized forms offer attractive options relative to alternatives that use conventional bulk hardware and fiber optic tethers. This work presents a technology of this type, based on microscale light-emitting diodes ( $\mu$ -ILEDs) and near-field communication (NFC) protocols, and optimized to activate photocaged morphine (pc-Mor) in targeted regions of the spinal cord. The unique flexible, lightweight designs ensure stable, minimally invasive operation in small animal model behavioral studies, with efficient power consumption and minimized thermal load on fragile tissues. Experimental results demonstrate effective pain suppression and

\* Corresponding author. Querrey Simpson Institute for Bioelectronics, Northwestern University, Evanston, IL, 60208, USA.

\*\* Corresponding author. Pharmacology Unit, Department of Pathology and Experimental Therapeutics, Faculty of Medicine and Health Sciences, Institute of Neurosciences, University of Barcelona, L'Hospitalet de Llobregat, 08907, Spain.

\*\*\* Corresponding author. Querrey Simpson Institute for Bioelectronics, Northwestern University, Evanston, IL, 60208, USA.

E-mail addresses: [y-huang@northwestern.edu](mailto:y-huang@northwestern.edu) (Y. Huang), [fciruela@ub.edu](mailto:fciruela@ub.edu) (F. Ciruela), [jrogers@northwestern.edu](mailto:jrogers@northwestern.edu) (J.A. Rogers).

<sup>1</sup> These authors contributed equally to this work.

<https://doi.org/10.1016/j.bios.2025.117440>

Received 19 December 2024; Received in revised form 26 February 2025; Accepted 1 April 2025

Available online 4 April 2025

0956-5663/© 2025 Elsevier B.V. All rights are reserved, including those for text and data mining, AI training, and similar technologies.

reduced opioid-related side effects in an animal model of pain, thereby establishing this platform as a promising solution for chronic pain management.

## 1. Introduction

Chronic pain, lasting 12 weeks or more, affects more than 600 million people worldwide (Dave, 2024; Rahman et al., 2023). Opioids, such as morphine, are commonly used to treat severe chronic pain (Nadeau et al., 2021). However, prolonged use can lead to complications, including increased tolerance, opioid-induced respiratory depression (OIRD), constipation (Vijayvargiya et al., 2020), complex opioid dependence (CPOD) (Manhapra et al., 2020), opioid-induced hyperalgesia (OIH), and neurotoxicity (OIN) (Mercadante, 2023). These issues underscore the need for safer and more effective alternatives to opioid therapy. Recent advances in light-based techniques for neuromodulation and pharmacology provide strategies to dramatically improve target specificity and spatiotemporal precision control, thus enabling comprehensive studies of neuronal circuits involved in pain perception and modulation (Iseppon and Arcangeletti, 2020; Lee and Kim, 2016; Li et al., 2024). Photopharmacology uses pharmacological agents that incorporate light-responsive molecular units engineered to undergo photolysis or photoisomerization upon exposure to specific wavelengths of light (Iseppon and Arcangeletti, 2020). These photoactivatable synthetic drugs provide the basis for precision schemes that minimize side effects and optimize therapeutic outcomes by harnessing light for precise spatiotemporal manipulation of physiological processes and behaviors without the need for optogenetic modifications (Hüll et al., 2018; Paoletti et al., 2019).

The use of photoactivatable drugs *in vivo* (e.g., spinal cord tissues), typically requires implantable fiber optic hardware for the delivery of light with suitable wavelengths from an external source to a targeted anatomical location (Bonin et al., 2016; McClain et al., 2023; Notartomaso et al., 2024; Taura et al., 2018). However, physical tethers and cable assembly structures can substantially constrain research paradigms by modifying natural behaviors, particularly when assessing and quantifying analgesic efficacy through observed changes in behaviors (Park et al., 2015; Samineni et al., 2017). Such approaches are also unlikely to translate effectively for use in humans, because of a range of practical and medical considerations. Miniaturized, wireless, battery-free, and fully implantable optical systems have the potential to bypass these limitations and, thus, to pair with photopharmacological agents as the basis for advanced, programmable pain management systems (Grajales-Reyes et al., 2021; Wu et al., 2022). This paper introduces an engineering platform that addresses this need, with demonstrated capabilities to optically modulate the pain circuitry at the dorsal spinal cord level in freely behaving small animal models, for safe and effective pain management. This technology also minimizes adverse side effects of typical morphine treatments and improves their efficacy at low exposure thresholds. Specifically, the device includes microscale inorganic light-emitting diodes ( $\mu$ -ILEDs) with an emission wavelength of 405 nm, wirelessly powered and controlled by near-field communication (NFC) technology to allow programmed photolysis of a photocaged form of morphine (pc-Mor). This setup enables remote activation of pc-Mor exclusively in target tissues of the dorsal horn, producing analgesic effects. The thin, flexible, small, and lightweight design of the device allows for seamless adhesion to the epidural space, ensuring mechanically robust operation throughout the implantation period. Further optimization of operating parameters (i.e., power, duty cycle, and pulsing frequency) guided by numerical simulations and experimental validations of electrical, optical, and thermal properties ensures strict compliance with the safety guidelines for potential heat generation from electrical heating and photothermal effects. The platform successfully demonstrates suppression of formalin-induced inflammatory nociceptive behaviors compared to standard morphine treatment in

acute cases. Furthermore, mice chronically treated with pc-Mor for two weeks do not show a significant reduction in analgesic efficacy, while mice treated with vehicle and morphine exhibit opioid-mediated adverse side effects within 5 days after treatment. Such chronic treatment studies and histological validations indicate that pc-Mor could support a promising, fully implantable option to bypass undesired opioid-based side effects for chronic pain management in various clinical settings.

## 2. Methods

### 2.1. Device fabrication

The fabrication began with laser ablation of a flexible printed circuit board (fPCB; PCBWay) with a layer stack of PI/Adhesive/Cu/PI/Cu/Adhesive/PI (12.5/15/18/25/18/15/12.5  $\mu$ m) based on a layout created using a commercial computer-aided design software (AutoCAD, Autodesk, Inc.). Filling drilled via holes by electroplating established an electrical connection between the top and bottom copper layers. The  $\mu$ -ILED, capacitors, and Schottky diodes joined with the contact pads of the fPCB with solder paste (CHIPQUIK, TS391AX10) applied with a hot air gun at 285 °C. An ultraviolet (UV) curable adhesive (Norland Optical Adhesive NOA 61; Norland Products) secured the solder joints for the  $\mu$ -ILED. A thin layer of PDMS encapsulated the solder joints for the capacitors and Schottky diodes. A chemical vapor deposition (CVD) process formed a conformal coating of parylene-C (10  $\mu$ m) on the surface of the device, as a biocompatible interface that protects against biofluids from the surrounding tissues. Detailed information about the electrical components is in Table S1.

### 2.2. Electrical and optical characterization

Characterization of the  $\mu$ -ILED began with current-voltage (IV) measurements performed using a semiconductor device analyzer (Keysight S1500A) and a probe station (Signatone 1160). A combination of an integrating sphere (OceanOptics), light source (OceanOptics), the  $\mu$ -ILED powered by a current source (Keithley 6221, Tektronix Inc.), and OceanView software provided the spectral power density ( $\mu$ W/nm) as a function of wavelength, allowing determination of the optical power of the  $\mu$ -ILED at varying applied currents (0.5, 0.6, 0.7, 0.8, 0.9, 1, 1.25, 1.5, 1.75, 2, 5, 10 mA). A customized MATLAB script yielded the total optical power by integrating the irradiance flux over the wavelength range from 340 nm to 1000 nm. A digital multimeter (Fluke 115) measured the voltage level across the wirelessly powered  $\mu$ -ILED located in the center of the behavior cage (H = 3.75 cm) as a function of applied primary antenna power ranging from 2 W to 10 W in 1 W intervals.

### 2.3. Animals and epidural implantation

Adult male CD-1 mice (Janvier Labs SL, Le Genest-Saint-Isle, France) bred in the animal facility of University of Barcelona (Campus of Bellvitge) weighing 25–35 g were used for these studies. The University of Barcelona Committee on Animal Use and Care (CEEA) approved the protocol and experiments were conducted under the authorization of the Catalan Government (126/22). Following the approved experimental protocol all animals were supervised daily to assess signs of adverse effects during treatment. Animals were housed and tested in compliance with the guidelines provided by the Guide for the Care and Use of Laboratory Animals and following the European Union directives (2010/63/EU). Mice were housed individually in standard cages with libitum access to food and water and maintained under a 12 h dark/light

cycle (starting at 7:30 a.m.), at 22 °C and 66 % humidity (standard conditions).

Implantation of the device was in the epidural space under the T13 vertebra (Fig. 1B) following an adapted procedure (Grajales-Reyes et al., 2021). Briefly, mice were anesthetized with 2.5 % isoflurane and placed sternal on an isothermal pad under a dissecting microscope to maintain body temperature. A longitudinal incision was made along the vertebral

column, from the middle rib cage to the pelvic girdle, taking care not to damage the underlying muscles. The T13 and L1 vertebrae were identified, and the superficial back muscles were carefully incised to expose the spinous processes and the dorsal surface of T13 and L1. Soft tissue was removed to reveal the dorsal spinal artery, which was continuously monitored for sharpness to prevent dura or spinal cord damage. Subsequently, the spinous process of the L1 vertebra was removed and any

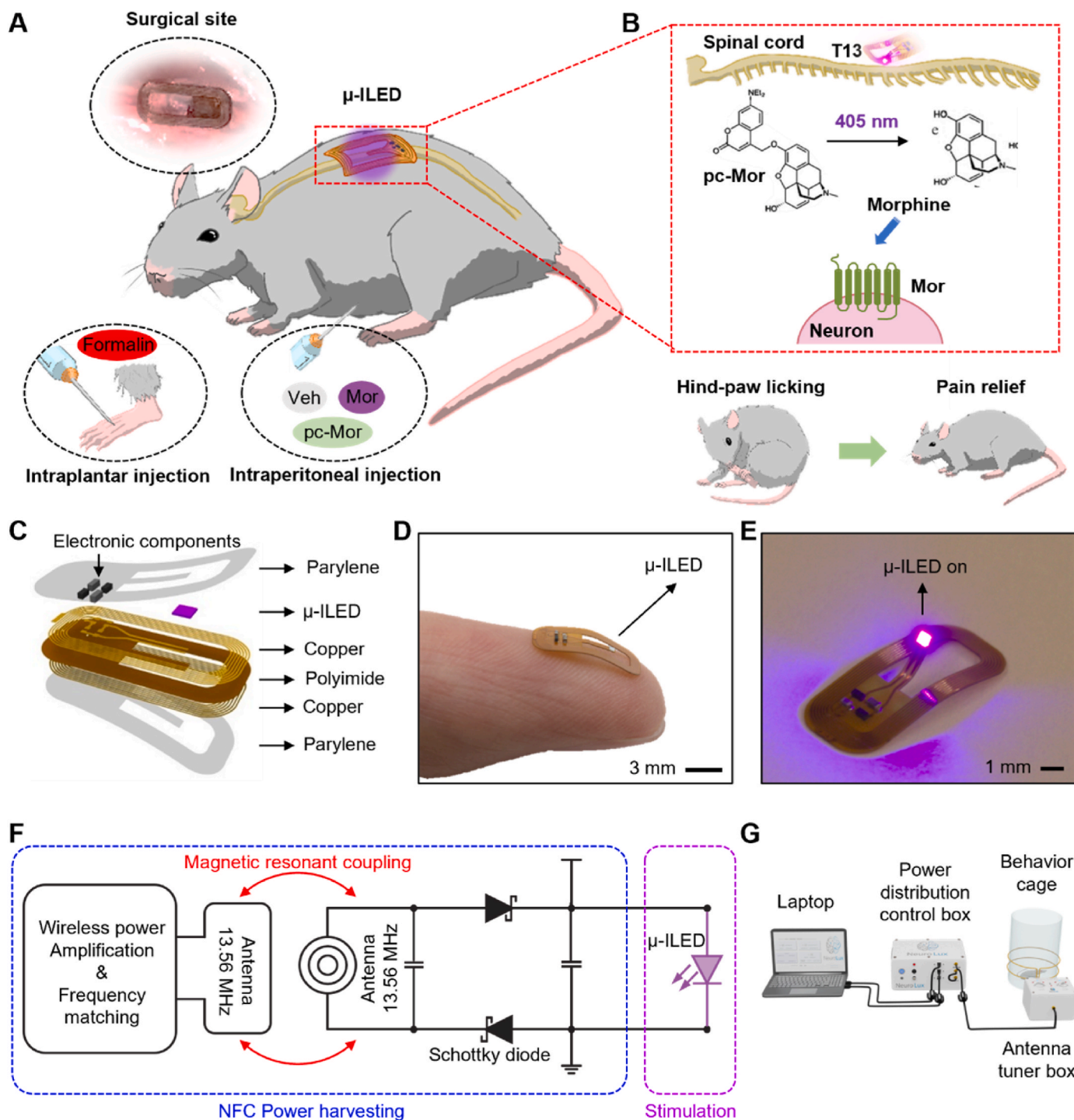


**Fig. 1.** Wireless, battery-free, photopharmacological pain management platform. Schematic illustration of the overall *in vivo* system operation (A) and photopharmacological pain management system on the spinal cord (B). The inset on the top left shows a schematic illustration of the surgical site, the inset on the bottom left shows an intraplantar injection of formalin, and the inset on the bottom middle shows an intraperitoneal injection of vehicle, morphine and photocaged-morphine. (C) Exploded illustration of a wireless, battery-free  $\mu$ -ILED implant. (D,E) Photographs of a flexible spinal implant with  $\mu$ -ILED being turned off (D) and on (E). (F) Electronic circuitry design for a wireless, battery-free  $\mu$ -ILED implant with a resonant frequency of 13.56 MHz for magnetic resonant coupling and near-field communication (NFC) power harvesting. (G) Illustration of experimental setups for *in vivo* experiment.

necessary bone fragments were removed from the caudal edge of T13 to ease  $\mu$ -ILED insertion. The spinal device was carefully placed under the T13 vertebra, and super glue gel was applied between the body of the device and the dorsal surface of L1 to ensure placement. After ensuring clear visualization of the surgical field, the skin edges were held with forceps and closed with 3/8 19 mm silk sutures. Post-surgical care included subcutaneous administration of warm saline and meloxicam for pain management over three days. Animal research and light stimulation was initiated 10 days after surgery (see Supporting Information).

### 3. Results

#### 3.1. Device design and operation

The *in vivo* photopharmacology strategy developed in this study uses a wirelessly powered, implantable microscale inorganic light emitting diode ( $\mu$ -ILED) in a design optimized to establish an interface with the spinal cord to illuminate a photocaged form of morphine (pc-Mor) (López-Cano et al., 2023). The result enables a light-programmable, safe and effective means for managing nociception with precise spatial and temporal resolution. Fig. 1A and B illustrate the overall concept. As an implantable light source that can remotely activate pc-Mor in the formalin murine model of pain (López-Cano et al., 2023), the  $\mu$ -ILED resides in the epidural anatomical space under the T13 vertebra (Fig. 1B). Implantation involves a surgical protocol configured to allow manipulation of spinal dorsal horn neurons (Fig. 1A top inset) (Grajales-Reyes et al., 2021). Detailed surgical procedures are in the Methods section. Assessment of antinociceptive efficacy relies on evaluations of behavioral nociceptive responses (i.e., hind-paw licking) after  $\mu$ -ILED irradiation of the dorsal horn region to uncage pc-Mor, which targets neurons of the central nervous system of the animal model of pain (Fig. 1A). Intraperitoneally administered pc-Mor, which in the absence of light illumination does not have biological effect, follows intraplantar delivery of a diluted formalin solution (Fig. 1A). The formalin solution triggers nociceptive behaviors such as licking and biting the injected hind paw. Quantification of these behaviors involves measuring their duration within 35 min after formalin injection. Irradiation of the spinal cord with 405 nm light from the  $\mu$ -ILED induces photolysis of the coumarin benzylic bond in pc-Mor, resulting in the release of morphine, which effectively targets spinal cord  $\mu$ -opioid receptors (MORs) and abolishes pro-nociceptive effects (Fig. 1B).

The device takes the form of a thin, flexible platform with an open, oblong geometry ( $11 \times 4.9 \times 0.116$  mm, L  $\times$  W  $\times$  H). This design enables spatiotemporal control of light delivery for drug activation, with lasting stability at its interface with the spinal cord. Fig. 1C and Table S1 present layer-by-layer information on device construction. The  $\mu$ -ILED, located at the flexible probe tip to facilitate manipulation during surgical procedures, emits light at a wavelength of 405 nm to trigger the photolysis of pc-Mor (Fig. 1D and E). A double-layered copper-polymer flexible printed circuit board (fPCB) defines the electrical circuits for wireless powering and control of the  $\mu$ -ILED. The coils for magnetic inductive coupling exploit a bilayer layout with seven turns per layer, each with a width and spacing of 75  $\mu$ m. The circuit employs a half-bridge rectifier configuration with two Schottky diodes, a smoothing capacitor, and a tuning capacitor to achieve power amplification, optimized impedance matching and efficient rectification for wireless power transfer (Fig. 1F). A coating of poly(dimethylsiloxane) and a UV-curable epoxy provide robust protection for the embedded electronic components and  $\mu$ -ILED. A thin layer of parylene-C uniformly encapsulates the entire surface of the device, to electrically isolate the system from surrounding biofluids (Fig. S1). Fig. S2 and Methods provide details on the fabrication processes. The power transfer utilizes near-field wireless communication (NFC) protocols operating at the industrial, scientific, and medical radio frequency band (ISMRF; 13.56 MHz) to supply power to the  $\mu$ -ILED through magnetic resonant coupling between the coils of the device and transmission antennas placed along the cage perimeter

(Fig. 1F). The setup includes a collection of external hardware and embedded software. The antenna tuner optimizes power transfer between the power distribution control (PDC; NeuroLux Inc.) box and the transmission antenna for maximum efficiency. Software with a graphical user interface configures the operational parameters, such as frequency and duty cycle of activation of the  $\mu$ -ILED (Fig. 1G).

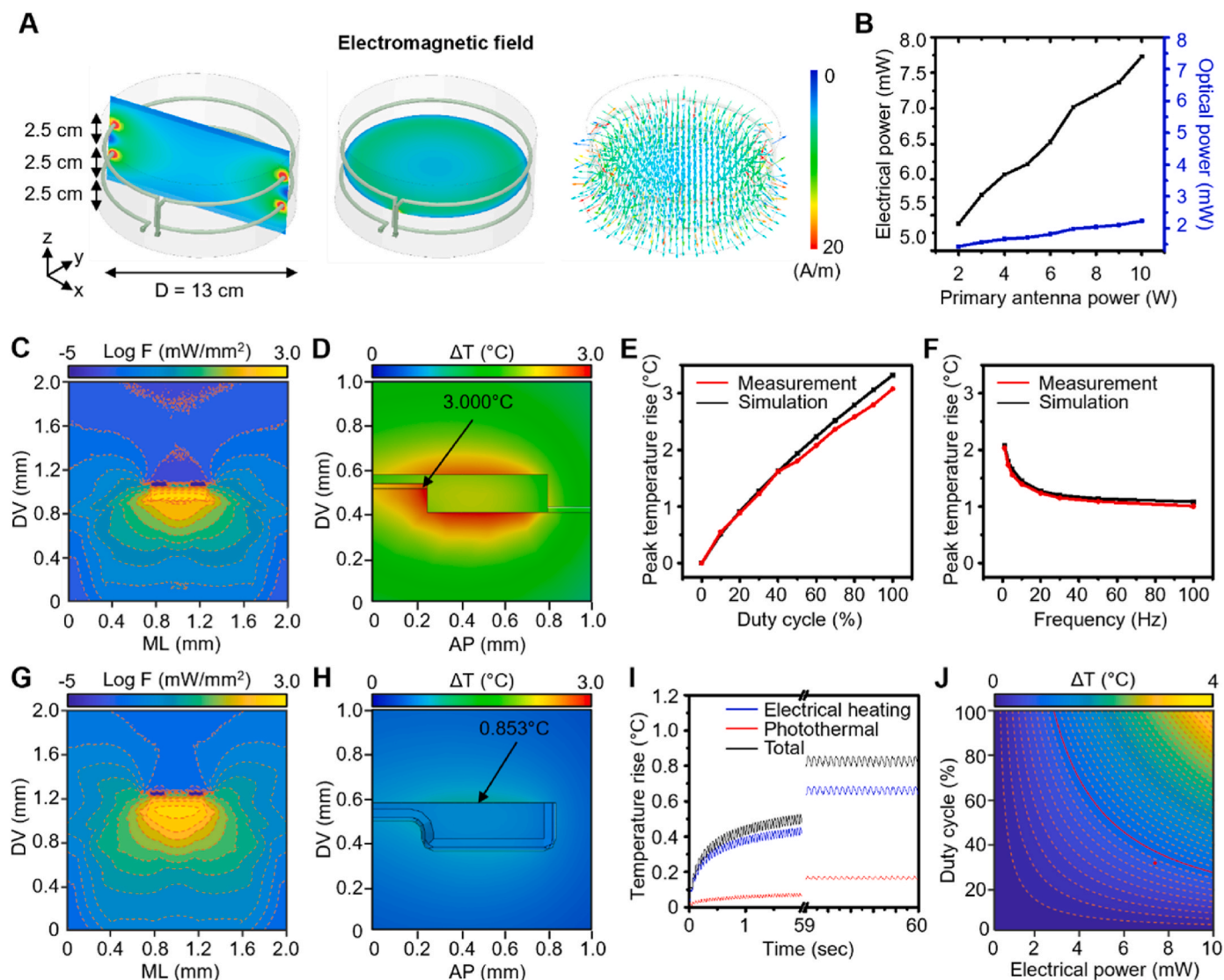
#### 3.2. Electromagnetic, optical, and thermal characteristics

Fig. 2A shows the magnetic field distribution throughout the animal behavioral enclosure (D = 13 cm, H = 19 cm). The field strength has a large gradient near the antenna wires but is relatively uniform in the middle plane, ensuring a steady power delivery to the  $\mu$ -ILED. Figs. S3A and B show that the power transfer efficiency (PTE) for the  $\mu$ -ILED decreases monotonically with a series load resistance due to the power consumed by the additional resistance. The PTE at the center position is larger than that at the corner position due to improved coupling behavior between the loops. Details of the simulations are in the Materials and Methods section. Fig. 2B presents the electrical and optical power of the  $\mu$ -ILED as a function of the power applied to the transmission antenna, with the device positioned in the center of the cage at a height of 3.75 cm. Combining the current-voltage characteristics of the  $\mu$ -ILED with the spectral power density plot (Fig. S4) yields the conversion ratio between electrical and optical power with respect to the power applied to the transmission antenna. Details on the electrical and optical characterization processes are in the Methods section.

Heat generation from the device could potentially alter physiological and behavioral outcomes. The heating follows from the electrical operation of the device and photothermal effects from light absorption by the tissue (Zhang et al., 2021). The studies to examine these effects involve an implantable  $\mu$ -ILED system with a microfabricated thin film temperature sensor (Fig. S5) attached to the surface of the  $\mu$ -ILED (Fig. S6A) for *in vivo* measurements during operation at two different levels of optical power (Fig. S8B; 1.56 mW, 2.5 °C (left) and 2.04 mW, 3.1 °C (right)). The results for these cases indicate increases in temperature that exceed a physiologically acceptable range (Yarmolenko et al., 2011; Zhang et al., 2019). Fig. 2E and F illustrate the dependence of the temperature increase on the duty cycle and frequency of the  $\mu$ -ILED. A numerical model yields calculated values for the temperature rise to compare to these experimental data (Fig. S6). The optical fluence rate contributes to the generation of heat in the form of the photothermal effect (Fig. 2C). Finite element analysis (FEA) captures the role of electrical heating (Fig. S7). Fig. 2D combines both electrical and photothermal effects. Measurement results and simulated data for four different cases are in excellent agreement (Fig. 2E and F, and Fig. S8B). Summaries of the geometrical parameters and thermal properties of the device, gray matter, white matter, and the surrounding tissue that serve as inputs to the models appear in Figs. S3, 6, 9, and 14A, and Tables S2 and 3).

Simulations show a peak temperature rise of 2.65 °C for the case of operation at a 100 % duty cycle at an optical power of 2.04 mW (Figs. S9 and 10). The peak temperature rise for the experimental parameters used in the behavioral experiments described later (30 % duty cycle, 20 Hz frequency, and 2.042 mW optical power) is 0.85 °C (Fig. 2G–I, and Figs. S11 and 12), indicating a value within the physiologically acceptable range (Efimov et al., 2024; Yang et al., 2021). The temperature decreases rapidly with depth into the tissue (Fig. S13). The contour heatmap shows the peak temperature rise as a function of duty cycle and electrical power at a frequency of 30 Hz (Fig. 2J). Simple modifications to the device design, such as an addition of a thin layer of copper (25  $\mu$ m) for heat spreading on the backside of the fPCB, can be implemented to further reduce the temperature rise (Fig. S14). Additional details on the simulations are in the Methods section.

The mechanical properties are also important. Figs. S15A–C show the results of numerical modeling of cyclic bending that can occur due to movements of the animal. The maximum equivalent strain induced in



**Fig. 2.** Characterization of the wirelessly operating spinal cord implant.

(A) Electromagnetic field intensity simulation results for the cylindrical behavior cage ( $D = 13$  cm,  $H = 18$  cm) with a double-loop antenna spaced 2.5 cm apart with primary antenna power of 8 W (Left: ZX plane, middle: YZ plane, right: whole area.). Only the height up to 7.5 cm is shown in the image. (B) Electrical and optical power for  $\mu$ -ILED as a function of primary antenna power. (C) Transverse section of 3D Monte Carlo modeling of optical fluence rate distribution in the spinal cord model containing gray matter, white matter, surrounding tissue,  $\mu$ -ILED implant, and temperature sensor (100 % duty cycle and optical power of 2.042 mW). (D) Sagittal section of finite element analysis (FEA) of overall temperature distribution in the spinal cord model containing gray matter, white matter, surrounding tissue,  $\mu$ -ILED implant, and temperature sensor (100 % duty cycle and optical power of 2.042 mW). (E) Measured and simulated temperature sensor peak temperature rise curves for an  $\mu$ -ILED probe as a function of duty cycle at a 20 Hz operating frequency. (F) Measured and simulated peak temperature rise for an  $\mu$ -ILED probe as a function of operating frequency at a 30 % duty cycle. (G) Transverse section from 3D Monte Carlo modeling of the optical fluence rate distribution in a spinal cord model containing gray matter, white matter, surrounding tissue and an  $\mu$ -ILED implant (30 % duty cycle, 20 Hz operating frequency, and optical power of 2.042 mW). (H) Sagittal section from finite element analysis (FEA) of the overall temperature distribution in a spinal cord model containing gray matter, white matter, surrounding tissue and an  $\mu$ -ILED implant (30 % duty cycle, 20 Hz operating frequency, and optical power of 2.042 mW). (I) Simulated peak temperature rise for the electrical heating effect, photothermal effect, and combined effect with 30 % duty cycle, 20 Hz operating frequency, and 2.042 mW optical power. (J) Contour heatmap showing the peak temperature rise for different duty cycles and electrical power levels. The red dashed line indicates the contour where  $\Delta T = 1$  °C. The maximum peak temperature rise in tissue for the working load is 0.853 °C. (For interpretation of the references to colour in this figure legend, the reader is referred to the Web version of this article.)

the top and bottom coils (Fig. S15C) for a device bent to a radius of curvature of 29 mm (Kathe et al., 2022), integrated on the PDMS substrate (15 mm  $\times$  30 mm  $\times$  4 mm), is 0.14 %, which is below the elastic limit of the copper (0.3 %). Measurements capture changes in the resistance of the coils over 10000 cycles of bending by applying a linear displacement set to achieve a maximum radius of curvature of 29 mm (Fig. S15D). The data indicate no measurable change in resistance (Fig. S15E). Details are in the Methods section.

### 3.3. Wireless $\mu$ -ILED-mediated pc-Mor photoactivation targets spinal cord MOR in an animal model of pain

Recent research demonstrates that remote, local photoactivation of morphine can produce analgesia without opioid-related adverse effects in animal models of pain (López-Cano et al., 2023). That initial report used a non-tunable high-intensity 405 nm LED to uncage morphine in the lumbar segment (L4–L6) of the spinal cord (behind the T13 vertebra) via targeted delivery through an epidurally implanted optical fiber.

Light pulses were administered at a frequency of 1 Hz, with an output power of 23 mW and an intensity of 2000 mA. Although these experimental conditions enable high anti-nociceptive efficacy, they also pose a significant risk of spinal cord damage due to the considerable invasiveness associated with the epidural approach. The work presented here provides comparable anti-nociceptive efficacy but with reduced optical power due to focused light delivery and with minimal epidural invasiveness.

First experiments examine the  $\mu$ -ILED-mediated pc-Mor photouncaging performance *in vitro* (Fig. 3A). Monitoring of the uncaging of morphine occurs in aqueous buffer using irradiation conditions like those intended for use in mice (2.1 mW for 60 min). Data show that subjecting a small volume of a 0.9 mM pc-Mor solution in PBS:DMSO 10:1 to these illumination conditions results in nearly complete release of morphine after 60 min as determined by HPLC measurements

(Fig. 3B), consistent with changes monitored by UV-vis absorption spectroscopy (Fig. S16). Thus, a 10-fold reduction in optical yield compared to previously described yields a comparable pc-Mor uncaging efficiency.

Further experiments demonstrate  $\mu$ -ILED-mediated pc-Mor photouncaging *in vivo* by monitoring its ability to photocontrol morphine-mediated antinociception in an animal model of pain. A formalin mouse model enables the evaluation of peripheral and central MOR-mediated antinociceptive effects (Mogil, 2009). Implanted mice are administered with vehicle, morphine or pc-Mor before assessing its antinociceptive effects in dark and light conditions (Fig. 3C). Hind paw formalin injection generates an innate licking/biting behavior, which is not modified upon vehicle administration, neither in dark nor in light conditions (Fig. 3D). Importantly, epidural irradiation produces a significant antinociceptive effect (Fig. 3D). A two-way ANOVA (treatment x

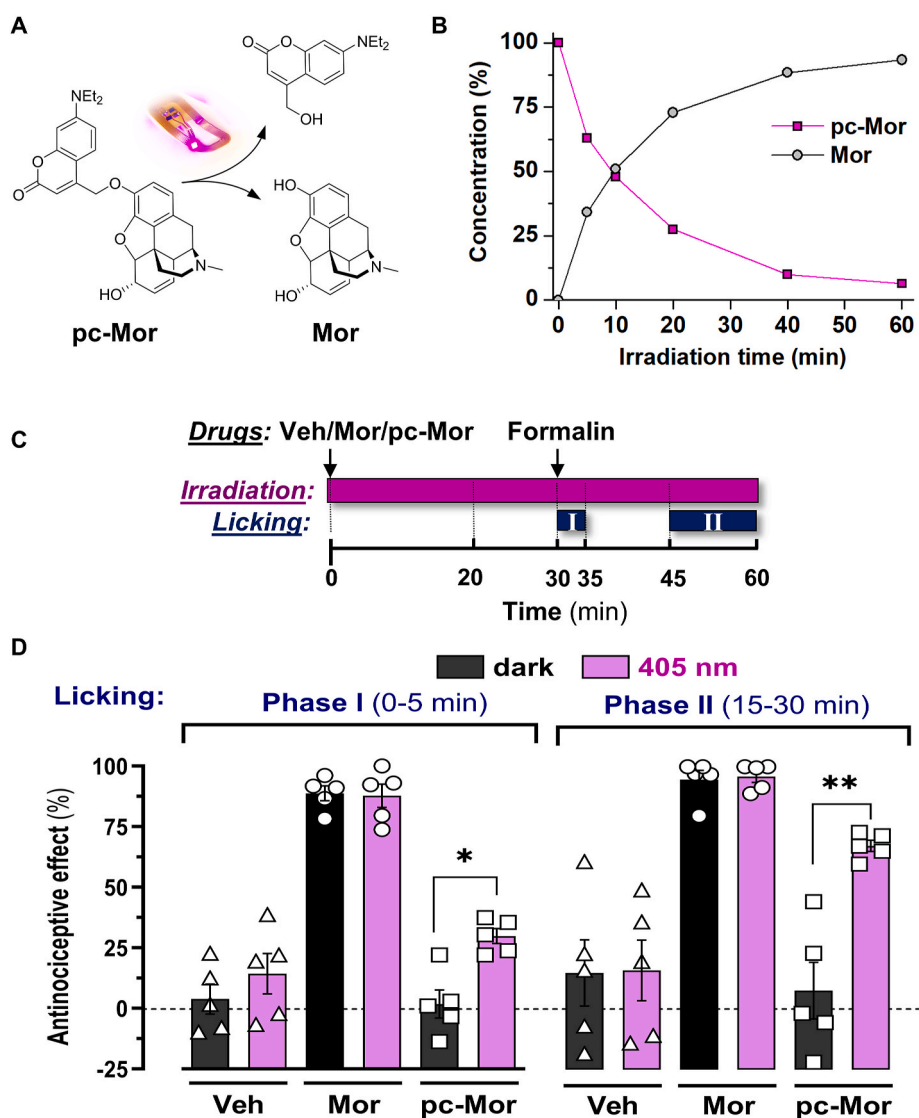


**Fig. 3.** Photouncaging of pc-Mor *in vitro* and *in vivo*. (A) Schematic representation of  $\mu$ -ILED-mediated pc-Mor photouncaging. (B) HPLC determination of the variation of the concentration of pc-Mor and morphine during the photouncaging process conducted in solution (100  $\mu$ L of PBS:DMSO 10:1) under  $\mu$ -ILED irradiation (2.1 mW). (C) Scheme of the 405 nm irradiation regime (violet rectangle) and licking recordings (blue rectangles – Phase I and Phase II) in the formalin animal model of pain. Animals implanted with the  $\mu$ -ILED device received an intraperitoneal injection of vehicle (Veh, saline), morphine, or pc-Mor (10 mg/kg, i.p.), followed immediately by the initiation of continuous 405 nm irradiation. The irradiation parameters consisted of a 1-h exposure with a 30 % duty cycle, 20 Hz frequency, and an optical power of 2.042 mW. (D) Optical control of spinal cord Mor in the formalin animal model of pain. Central light-dependent pc-Mor-mediated antinociception in  $\mu$ -ILED implanted mice was assessed upon irradiation of the spinal cord (see Fig. 1 a). Total hind paw licking was measured for 0–5 min (phase I) and 15–30 min (phase II) after intraplantar injection of 20  $\mu$ l of formalin solution (2.5 % paraformaldehyde). The antinociceptive effect was calculated as the percentage of the maximum possible effect and expressed as mean  $\pm$  SEM (n = 5). \*P < 0.05, \*\*P < 0.01, \*\*\*P < 0.001, \*\*\*\*P < 0.0001, two-way ANOVA with Tukey's post hoc test. (For interpretation of the references to colour in this figure legend, the reader is referred to the Web version of this article.)

illumination) confirms a significant main effect of treatment (Phase I:  $F_{(2, 24)} = 126.2$ ,  $P < 0.0001$ ; Phase II:  $F_{(2, 24)} = 40.3$ ,  $P < 0.0001$ ), illumination (Phase I:  $F_{(1, 24)} = 7.676$ ,  $P = 0.0106$ ; Phase II:  $F_{(1, 24)} = 7.601$ ,  $P = 0.0110$ ) and the interaction between both factors (Phase I:  $F_{(2, 24)} = 3.51$ ,  $P = 0.046$ ; Phase II:  $F_{(2, 24)} = 6.764$ ,  $P = 0.0047$ ). Morphine (10 mg/kg, i.p.) exerts antinociceptive effects both at phases I and II, regardless of light irradiation (Fig. 3D). Interestingly, pc-Mor (10

mg/kg, i.p.) is only able to suppress formalin-induced nociceptive behavior when light is delivered to the epidural anatomical space through the  $\mu$ -ILED device (Fig. 3D). Thus, while pc-Mor does not display antinociceptive effects in dark conditions, it reduces nociception both in phase I ( $29.8 \pm 3\%$ ) and in phase II ( $67.4 \pm 2.3\%$ ) upon direct spinal cord illumination, with a Tukey's post-hoc test corroborating the observed antinociceptive effect ( $P = 0.0164$  and  $P = 0.0015$ ,

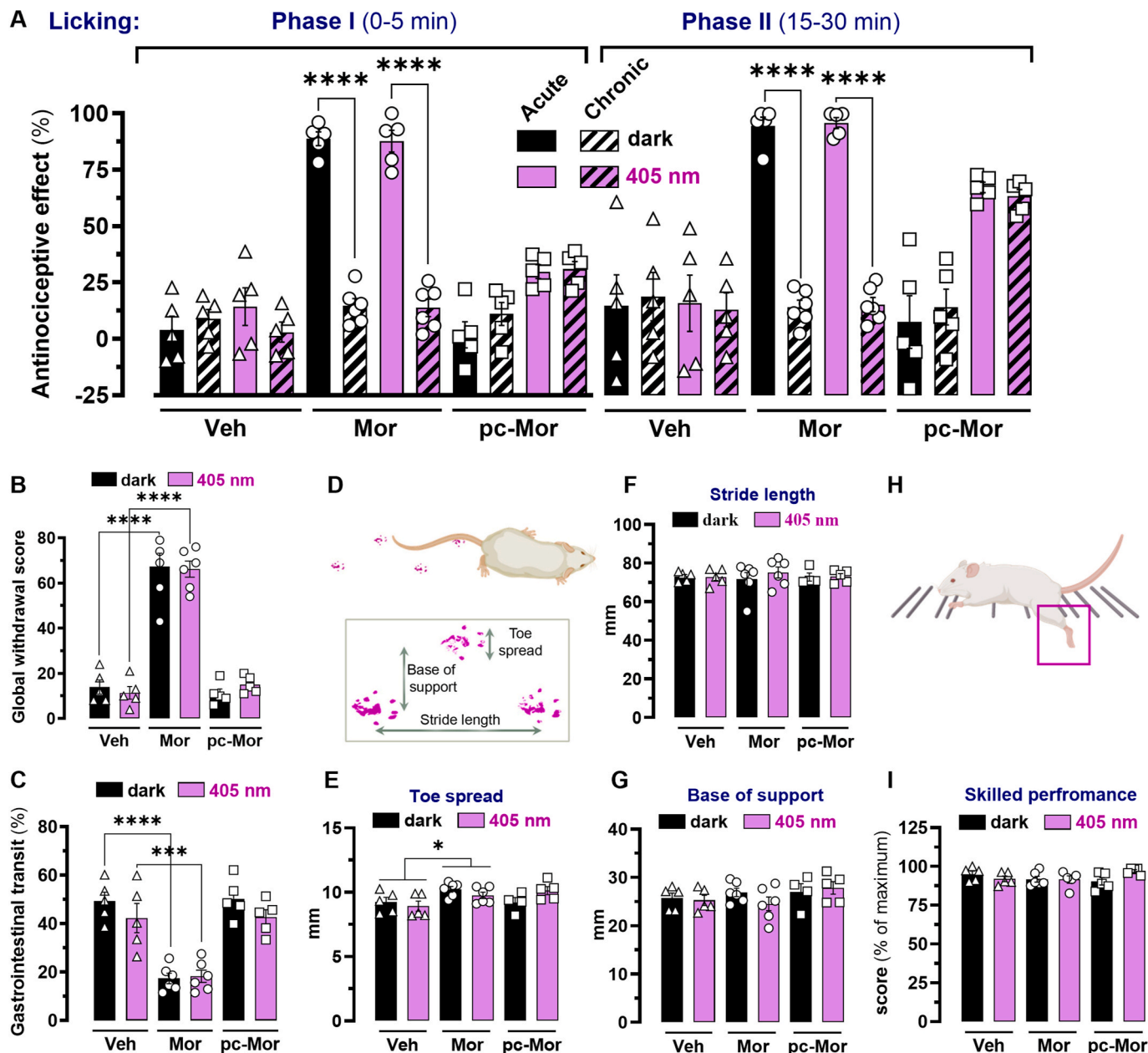


**Fig. 4.** Optical control of spinal cord Mor in the formalin animal model of pain without opioid-induced side effects. (A) Reduced opioid-induced tolerance upon morphine photocontrol. Animals implanted with the  $\mu$ -ILED device were chronically (twice a day for 5 days) administered with vehicle (Veh, saline, i.p.), morphine or pc-Mor (10 mg/kg, i.p.) 20 min before light irradiation (see Fig. 3c). Finally, on the last day of treatment, antinociception was determined as described in panel a) and the results compared with that obtained upon acute treatment. Data are expressed as mean  $\pm$  SEM ( $n = 5-6$ ). \*\*\*\* $P < 0.0001$ , three-way ANOVA with Tukey's post hoc test. (B) Naloxone precipitated morphine withdrawal.  $\mu$ -ILED animals were chronically treated, and light irradiated as described in panel a). After last drug administration, withdrawal was precipitated by administering naloxone (1 mg/kg, s.c.) and the global withdrawal score was calculated considering all the physical signs (i.e., wet dog shakes, jumping, paw tremor, sniffing, teeth chattering, piloerection, ptosis, diarrhea, tremor and/or decreased locomotor activity) and expressed as mean  $\pm$  SEM ( $n = 5-6$ ). \*\*\*\* $P < 0.0001$ , two-way ANOVA with Tukey's post hoc test. (C) Gastrointestinal transit (GIT) assessment. Animals were chronically treated, and light irradiated as in (D). Results are represented as percentage of activated charcoal transit according to total length of intestine (see Methods) and expressed as mean  $\pm$  SEM ( $n = 5-6$ ). Gait assessment through footprint analysis was performed after the completion of treatment and antinociception tests using the walking track (D). Paw prints were manually measured to determine toe spread (E), stride length (F), and base of support (G). Data are expressed as mean  $\pm$  SEM ( $n = 5-6$ ). \*\*\*\* $P < 0.0001$ , two-way ANOVA with Tukey's post hoc test. (E) Skilled locomotion was assessed using the horizontal ladder (H), where the positioning of both hind paws was evaluated using a standardized score normalized against the maximum possible score (I). Data are expressed as mean  $\pm$  SEM ( $n = 5-6$ ).

respectively). Interestingly, epidural uncaged pc-Mor has comparable efficacy to systemic morphine in phase II ( $P = 0.273$ ). These results demonstrate that pc-Mor is effective in mediating antinociception upon spinal cord  $\mu$ -ILED irradiation, thus representing a valuable strategy for the treatment of pain-related diseases.

### 3.4. $\mu$ -ILED pc-Mor photouncaging prevents tolerance and opioid side effects in a mouse pain model

Opioid-based analgesic therapies can lead to tolerance to their analgesic effects, as well as to a range of adverse consequences, including constipation, dependency, and addiction (Grim et al., 2020). Additional experiments explore the ability of the  $\mu$ -ILED-based morphine photopharmacology approach to mitigate some of these undesirable outcomes. The first studies examine the possible tolerance to the analgesic effects of chronic pc-Mor treatment compared to morphine-induced treatment. Here, mice are chronically treated with vehicle, morphine, or pc-Mor prior to evaluating formalin-induced behavior under dark and light conditions. A three-way ANOVA (treatment  $\times$  illumination  $\times$  drug regime) confirms a significant main effect of treatment (Phase I:  $F_{(2, 50)} = 92.9$ ,  $P < 0.0001$ ; Phase II:  $F_{(2, 50)} = 25.89$ ,  $P < 0.0001$ ), illumination (Phase I:  $F_{(1, 50)} = 9.326$ ,  $P = 0.0001$ ; Phase II:  $F_{(1, 50)} = 33.95$ ,  $P < 0.0001$ ), drug regime (Phase I:  $F_{(1, 50)} = 75.5$ ,  $P < 0.0036$ ; Phase II:  $F_{(1, 50)} = 15.58$ ,  $P = 0.0002$ ), the interaction between treatment and illumination (Phase I:  $F_{(2, 50)} = 85.32$ ,  $P < 0.0001$ ; Phase II:  $F_{(2, 50)} = 37.5$ ,  $P < 0.0001$ ) and the interaction between treatment and drug regime (Phase I:  $F_{(2, 50)} = 7.957$ ,  $P = 0.001$ ; Phase II:  $F_{(2, 50)} = 16.39$ ,  $P < 0.0001$ ), but not between the drug regime and illumination (Phase I:  $F_{(1, 50)} = 2.172$ ,  $P = 0.1468$ ; Phase II:  $F_{(1, 50)} = 0.4191$ ,  $P = 0.5203$ ) or treatment, illumination, and drug regime (Phase I:  $F_{(2, 50)} = 0.7647$ ,  $P = 0.4708$ ; Phase II:  $F_{(2, 50)} = 0.12$ ,  $P = 0.8872$ ) in both phases of the formalin test. As expected, chronic administration of morphine leads to the development of tolerance to its antinociceptive effects. Therefore, the Tukey post hoc test reveals a significant reduction ( $P < 0.0001$ ) of morphine antinociceptive effects after its chronic administration in phase I and II both under light and dark conditions (Fig. 4A). Importantly, chronic treatment with pc-Mor does not lead to tolerance, as no significant differences in antinociceptive effects are found between acute and chronic animals treated with pc-Mor in phases I and II, both under light and dark conditions (Fig. 4A).

In parallel, further experiments evaluate the development of withdrawal syndrome (Fig. 4B), an important adverse effect associated with chronic opioid use. Mice receiving daily drug injections (i.e., vehicle, morphine, or pc-Mor) are subsequently administered naloxone (1 mg/kg) to precipitate withdrawal. A significant effect of drug treatment is identified by two-way ANOVA ( $F_{(2, 26)} = 146.5$ ,  $P < 0.0001$ ), whereas no significant effect of illumination ( $F_{(1, 26)} = 0.0006$ ,  $P = 0.9799$ ) or the interaction between both factors ( $F_{(2, 24)} = 0.4101$ ,  $P = 0.6678$ ) is observed. During behavioral observations conducted before naloxone administration, no withdrawal symptoms appear in any group of mice. Furthermore, the administration of naloxone does not produce any significant effects in the mice that received the vehicle. Notably, in mice treated chronically with morphine, the injection of naloxone induces a pronounced withdrawal syndrome characterized by multiple somatic symptoms (i.e., wet dog shakes, paw tremor, jumps, ptosis, decreased locomotor activity, diarrhea). In contrast, mice subjected to chronic pc-Mor treatment do not show withdrawal syndrome (Fig. 4B).

Other experiments evaluate the ability of pc-Mor to induce constipation, a notably adverse effect commonly reported by patients in association with chronic opioid use and withdrawal (Farmer et al., 2018). To this end, gastrointestinal transit (GIT) was assessed in mice following systemic administration of vehicle, morphine, or pc-Mor. Indeed, morphine produces a marked light-independent inhibition of GIT, as expected (Fig. 4C). A significant effect of treatment is identified by a two-way ANOVA ( $F_{(2, 26)} = 43.75$ ,  $P < 0.0001$ ), whereas no significant effect of illumination ( $F_{(1, 26)} = 2.44$ ,  $P = 0.1304$ ) or the

interaction between both factors ( $F_{(2, 26)} = 0.9136$ ,  $P = 0.4136$ ) is observed. Importantly, while Tukey's post-hoc test reveals a significant inhibition of GIT in morphine administered animals both in dark and upon spinal cord irradiation ( $P < 0.0001$  and  $P < 0.001$ , respectively), pc-Mor does not produce a change in GIT, neither in dark ( $P > 0.9999$ ) nor under light ( $P > 0.9999$ ) conditions (Fig. 4C).

Finally, to assess the impact of  $\mu$ -ILED device implantation surgery or possible irradiation-induced spinal cord dysfunction, gait and skilled locomotion evaluations are examined to determine functional outcomes. In the footprint analysis (Fig. 4D), the gait parameters including toe spread (Fig. 4E), stride length (Fig. 4F), and base of support (Fig. 4G) determine the stability and consistency of regular locomotion between groups. The toe spread shows minor variation between the animals treated with vehicle and morphine-treated animals (Fig. 4E). However, this difference is within the expected range of normal variability and is independent of light exposure. Both the stride length (Fig. 4F) and the base of support (Fig. 4G) remain consistent in all treatments, with no significant changes between conditions with and without light delivery. These findings indicate that light delivery through the spinal cord device does not alter gait parameters, confirming that the implanted device and light exposure have no adverse impact on sensorimotor functions required for stable and symmetric gait.

In the horizontal ladder test (Fig. 4H), the accuracy of the placement of the paw during skilled locomotion provides additional data to determine whether the implanted device or the delivery of light affects sensorimotor function in a more challenging task. Accurate placement requires intact proprioception, effective descending motor commands from the supraspinal centers to the spinal cord, and reliable ascending sensory feedback. In all groups, scores are close to maximum performance, with no significant differences between animals exposed to light and those not exposed (Fig. 4I), indicating that light delivery does not interfere with sensorimotor function. Additionally, these scores are within the normal range for unimplanted animals and comparable to those recorded before device implantation (data not shown), suggesting that neither the device implanted in contact with the dorsal horns of the spinal cord nor light delivery impaired skilled locomotion. Taken together, these data provide promising evidence for a wireless, battery-free  $\mu$ -ILED-mediated opioid-based treatment with effective analgesic effects while minimizing adverse side effects and, importantly, preventing the development of analgesic tolerance.

## 4. Discussion

The use of opioids for pain relief raises significant pharmacotherapeutic concerns. Potential development of tolerance to its analgesic effects represents an important limitation, together with constipation, nausea, sedation, and respiratory depression as adverse side effects. The most alarming concern, however, is the risk of dependence and addiction, which can lead to misuse, overdose, and long-term health complications. These challenges are of increasing importance due to high prescription rates, making opioid-related side effects a major public health problem (Volkow and McLellan, 2016). These considerations motivate efforts to improve the safety of opioid use through approaches that deliver active opioids directly to the site of action with high precision. This paper presents a pharmacological strategy that relies on a wireless, battery-free, implantable  $\mu$ -ILED system for remote photoactivation of a caged-morphine derivative in the spinal cord of an animal model of pain. This technology effectively reduces the canonical physiological adverse effects of systemic opioid administration while preserving the full analgesic efficacy of morphine, offering a promising pathway to safer pain treatment.

The handling of opioid-induced side effects is essential for improving patient quality of life and preventing long-term complications. Beyond symptomatic treatment of adverse effects, several strategies can be used to mitigate them. These include switching to a different opioid with potentially fewer side effects, reducing the dose to minimize the risk of

toxicity, and altering the route of administration to minimize drug tolerance and increase efficacy (Rogers et al., 2013). Intrathecal drug delivery (IDD) of opioids, such as morphine and fentanyl, is effective for both nociceptive and neuropathic pain syndromes (De Andres et al., 2022). Interestingly, opioid IDD is increasingly used to manage chronic pain, particularly when conventional treatments, including oral medications, have failed (i.e., refractory pain) or come with undesirable side effects. Risks of opioid infusion include opioid-induced hyperalgesia, hormonal changes, peripheral edema, and pruritus and eventually also constipation, respiratory depression, and tolerance (De Andres et al., 2022). In addition, technical complications can arise, including intraoperative issues with the catheter entry site and pump placement location, as well as postoperative complications such as catheter migration, occlusion, leakage, or fracture. Furthermore, high local concentrations of opioids can promote the formation of granulomas at the tip of the catheter, potentially leading to neurological complications.

The  $\mu$ -ILED-mediated opioid-based treatment used here shows effective antinociceptive action while minimizing adverse side effects and, more importantly, preventing the development of analgesic tolerance. The wireless nature of this system significantly reduces the invasiveness commonly associated with tethered devices. This advance eliminates the need for implantation of an optical fiber throughout the epidural space (from the neck to the corresponding lumbar segment), as described recently (López-Cano et al., 2023). Consequently, by removing this requirement, the simplified surgical procedure and robust design of wireless implants minimize risks such as mechanical damage and inflammation of surrounding tissues, thus ensuring consistent light irradiation over extended periods while improving animal comfort. Additionally, the system enhances the safety profile by incorporating a reduced optical exposure threshold, which minimizes potential phototoxicity and thermal effects. This feature is crucial for long-term light-based therapies, as excessive or prolonged exposure to light can lead to tissue overheating, cellular damage, inflammation, or fibrosis. Beyond safety considerations, this wireless approach offers several experimental advantages as it enhances animal welfare by allowing unrestricted movement. Collectively, the  $\mu$ -ILED-based morphine photorelease improves overall safety, efficacy, and reliability of spinal cord opioid interventions while reducing the risk of common opioid adverse side effects.

For successful clinical translation, several important considerations must be addressed. One major challenge is ensuring the long-term biocompatibility and functional stability of the implant. Although the device includes a thin layer of parylene C as a biocompatible barrier for corrosion resistance, studies using this or similar biomaterials can lead to fibrotic encapsulation at 2 weeks, continuing to thicken until at least 16 weeks in rodents (de la Oliva et al., 2018; del Valle et al., 2015). Fibrotic layers of 50–100  $\mu$ m thickness are possible, which can attenuate blue light by approximately 10–15 %, based on the general optical properties of biological tissues and their scattering behaviour (Sanchez-Cano et al., 2020). To mitigate these effects, future studies could evaluate surface treatments such as dexamethasone-loaded coatings or hydrophilic modifications (Kim et al., 2008; Zhong and Belamkonda, 2007) designed to reduce inflammatory responses and delay capsule formation. These strategies can maintain optimal light transmittance for effective photouncaging over extended implant durations. For clinical translation, the system must also be adapted to the spinal anatomy of humans. As such, the  $\mu$ -ILED may need to be scaled up or implemented in arrays to achieve sufficient irradiance over large, deep target areas. In addition, a wearable, battery-powered NFC wireless power and control unit can be adapted to ensure the angular independency and precise alignment of the wireless power system (Choi et al., 2022). Increasing the light-emitting surface may increase the thermal load; however, our finite element analysis shows a peak temperature increase of  $\sim 0.85$  °C under typical operating conditions, suggesting that a safe thermal margin remains. If necessary, further design modifications, such as the implementation of highly conformable neural

implants, including flexible substrates and distributed components (Stieglitz et al., 2023) or the integration of a copper heat-spreading layer, could help maintain safe thermal limits (Miziev et al., 2024; Yarmolenko et al., 2011). In parallel, the regulatory pathway for such an implant requires extensive preclinical validation in larger animal models (e.g., sheep, nonhuman primates) to monitor chronic tissue response, encapsulation, and device stability over several months. These studies should include the monitoring of biomarkers of inflammation (e.g., TNF- $\alpha$ , IL-1 $\beta$ ) and functional assessments of light transmission through any encapsulating tissue. The accumulated preclinical data will form the basis for future clinical trials, ensuring that our device meets the safety and efficacy requirements before human use.

## 5. Conclusion

The use of wireless technology with photopharmacology significantly enhances pharmacological precision and safety. The combination of advanced drug design and innovative illumination systems has the potential to revolutionize pain management, offering a promising solution to reduce opioid dependency, thus addressing a major public health concern. Finally, from a translational perspective, flexible, biocompatible, battery-free, and wireless implants could be developed to treat chronic pain in patients resistant to conventional therapies. While the system demonstrates promise, several challenges remain, including those related to fibrotic encapsulation and thermal management. Future work may include appropriate surface treatments, scaling up processes for human trials, and robust pre-clinical validations to ensure long-term stability and safety. Such systems have the potential to disrupt pain management strategies by offering safer, more targeted treatment strategies.

## CRedit authorship contribution statement

**Minsung Kim:** Writing – review & editing, Writing – original draft, Visualization, Validation, Software, Resources, Project administration, Methodology, Investigation, Formal analysis, Data curation, Conceptualization. **Marc López-Cano:** Writing – review & editing, Writing – original draft, Visualization, Validation, Software, Resources, Project administration, Methodology, Investigation, Formal analysis, Data curation, Conceptualization. **Kaiqing Zhang:** Writing – review & editing, Writing – original draft, Visualization, Validation, Software, Methodology, Investigation, Formal analysis, Data curation, Conceptualization. **Yue Wang:** Writing – original draft, Visualization, Validation, Software, Methodology, Investigation. **Xavier Gómez-Santacana:** Writing – original draft, Validation, Methodology, Investigation, Data curation. **África Flores:** Writing – review & editing, Writing – original draft, Validation, Methodology, Investigation, Data curation. **Mingzheng Wu:** Visualization, Software, Methodology, Investigation, Formal analysis. **Shupeng Li:** Writing – original draft, Visualization, Validation, Methodology, Investigation, Formal analysis, Data curation. **Haohui Zhang:** Visualization, Validation, Methodology, Investigation, Formal analysis, Data curation. **Yuanting Wei:** Visualization, Methodology, Investigation, Data curation, Conceptualization. **Xiuyuan Li:** Visualization, Methodology, Investigation, Formal analysis, Data curation. **Cameron H. Good:** Validation, Conceptualization. **Anthony R. Banks:** Validation, Conceptualization. **Amadeu Llebaria:** Writing – review & editing, Writing – original draft, Validation, Supervision, Conceptualization. **Jordi Hernando:** Writing – review & editing, Writing – original draft, Visualization, Validation, Supervision, Software, Resources, Project administration, Methodology, Investigation, Funding acquisition, Formal analysis, Data curation, Conceptualization. **Sung-Hyuk Sunwoo:** Visualization. **Jianyu Gu:** Methodology. **Yonggang Huang:** Validation, Supervision, Methodology, Investigation, Funding acquisition, Formal analysis, Data curation, Conceptualization. **Francisco Ciruela:** Writing – review & editing, Writing – original draft, Visualization, Validation, Supervision, Resources, Project

administration, Methodology, Investigation, Funding acquisition, Formal analysis, Data curation, Conceptualization. **John A. Rogers:** Writing – review & editing, Writing – original draft, Visualization, Validation, Supervision, Resources, Project administration, Methodology, Investigation, Funding acquisition, Formal analysis, Data curation, Conceptualization.

### Data and materials availability

All data are available in the manuscript or the supplementary materials on request.

### Funding

This work was funded by the Querrey-Simpson Institute for Bioelectronics. This work was also supported by FEDER/Ministerio de Ciencia, Innovación y Universidades-Agencia Estatal de Investigación (PID2023-147425OB-I00 to FC, PID2020-120499RB-I00 to AL) and Agència de Gestió d'Ajuts Universitaris i de Recerca (AGAUR) - Generalitat de Catalunya (projects 2021 SGR 00698 to FC, 2021 SGR 00064 to JH, 2021 SGR 00508 to AL).

### Declaration of competing interest

The authors declare that they have no known competing financial interests or personal relationships that could have appeared to influence the work reported in this paper.

### Acknowledgments

We thank the Querrey-Simpson Institute for Bioelectronics. And we thank Centres de Recerca de Catalunya (CERCA) Programme/Generalitat de Catalunya for IDIBELL institutional support and Maria de Maeztu MDM-2017-0729 to Institut de Neurociències, Universitat de Barcelona.

### Appendix A. Supplementary data

Supplementary data to this article can be found online at <https://doi.org/10.1016/j.bios.2025.117440>.

### Data availability

Data will be made available on request.

### References

- Bonin, R.P., Wang, F., Desrochers-Couture, M., Ga, secka, A., Boulanger, M.-E., Côté, D. C., De Koninck, Y., 2016. *Mol. Pain* 12. <https://doi.org/10.1177/1744806916629051>.
- Choi, Y.S., Jeong, H., Yin, R.T., Avila, R., Pfenniger, A., Yoo, J., Lee, J.Y., Tzavelis, A., Lee, Y.J., Chen, S.W., Knight, H.S., Kim, S., Ahn, H.-Y., Wickerson, G., Vázquez-Guardado, A., Higbee-Dempsey, E., Russo, B.A., Napolitano, M.A., Holleran, T.J., Razzak, L.A., Miniovich, A.N., Lee, G., Geist, B., Kim, B., Han, S., Brennan, J.A., Aras, K., Kwak, S.S., Kim, J., Waters, E.A., Yang, X., Burrell, A., San Chun, K., Liu, C., Wu, C., Rwei, A.Y., Spann, A.N., Banks, A., Johnson, D., Zhang, Z.J., Haney, C.R., Jin, S.H., Sahakian, A.V., Huang, Y., Trachiotis, G.D., Knight, B.P., Arora, R.K., Efimov, I.R., Rogers, J.A., 2022. *Science* 376, 1006–1012. <https://doi.org/10.1126/science.abm1703>, 1979.
- Dave, P., 2024. *Asian J. of Hospital Pharmacy* 28–33. <https://doi.org/10.38022/ajhp.v4i2.84>.
- De Andres, J., Hayek, S., Perruchoud, C., Lawrence, M.M., Reina, M.A., De Andres-Serrano, C., Rubio-Haro, R., Hunt, M., Yaksh, T.L., 2022. *Fron. in Pain Res.* 3. <https://doi.org/10.3389/fpain.2022.900566>.
- de la Oliva, N., Mueller, M., Stieglitz, T., Navarro, X., de la Valle, J., 2018. *Sci. Rep.* 8, 5965. <https://doi.org/10.1038/s41598-018-24502-z>.
- del Valle, J., de la Oliva, N., Muller, M., Stieglitz, T., Navarro, X., 2015. 2015 7th International IEEE/EMBS Conference on Neural Engineering (NER). IEEE, pp. 442–445. <https://doi.org/10.1109/NER.2015.7146654>.
- Efimov, A.I., Hibberd, T.J., Wang, Y., Wu, M., Zhang, K., Ting, K., Madhupathy, S., Lee, M.-K., Kim, J., Kang, J., Riahi, M., Zhang, H., Travis, L., Govier, E.J., Yang, L., Kelly, N., Huang, Y., Vázquez-Guardado, A., Spencer, N.J., Rogers, J.A., 2024. *Biosens. Bioelectron.* 258, 116298. <https://doi.org/10.1016/j.bios.2024.116298>.

- Farmer, A.D., Holt, C.B., Downes, T.J., Ruggeri, E., Del Vecchio, S., De Giorgio, R., 2018. *Lancet Gastroenterol Hepatol* 3, 203–212. [https://doi.org/10.1016/S2468-1253\(18\)30008-6](https://doi.org/10.1016/S2468-1253(18)30008-6).
- Grajales-Reyes, J.G., Copits, B.A., Lie, F., Yu, Y., Avila, R., Vogt, S.K., Huang, Y., Banks, A.R., Rogers, J.A., Gereau, R.W., Golden, J.P., 2021. *Nat. Protoc.* 16, 3072–3088. <https://doi.org/10.1038/s41596-021-00532-2>.
- Grim, T.W., Acevedo-Canabal, A., Bohn, L.M., 2020. *Biol. Psychiatry* 87, 15–21. <https://doi.org/10.1016/j.biopsych.2019.10.020>.
- Hüll, K., Morstein, J., Trauner, D., 2018. *Chem. Rev.* 118, 10710–10747. <https://doi.org/10.1021/acs.chemrev.8b00037>.
- Iseppon, F., Arcangeletti, M., 2020. *STEMedicine* 1, e43. <https://doi.org/10.37175/stemedicine.v1i3.43>.
- Kathe, C., Michoud, F., Schönle, P., Rowald, A., Brun, N., Ravier, J., Furfaro, I., Paggi, V., Kim, K., Soloukey, S., Asboth, L., Hutson, T.H., Jelescu, I., Philippides, A., Alwahaab, N., Gandar, J., Huber, D., De Zeeuw, C.I., Barraud, Q., Huang, Q., Lacour, S.P., Courtine, G., 2022. *Nat. Biotechnol.* 40, 198–208. <https://doi.org/10.1038/s41587-021-01019-x>.
- Kim, D.-H., Richardson-Burns, S., Povlich, L., Abidian, M.R., Spanninga, S., Hendricks, J. L., Martin, D.C., 2008. In: *Indwelling Neural Implants: Strategies for Contending with the in Vivo Environment*. CRC Press/Taylor & Francis, Boca Raton (FL). Chapter 7.
- Lee, G.H., Kim, S.S., 2016. *Mediat. Inflamm.* 2016, 1–11. <https://doi.org/10.1155/2016/5808215>.
- Li, J., Che, Z., Wan, X., Manshah, F., Xu, J., Chen, J., 2024. *Biomaterials* 304, 122421. <https://doi.org/10.1016/j.biomaterials.2023.122421>.
- López-Cano, M., Font, J., Aso, E., Sahlholm, K., Cabré, G., Giraldo, J., De Koninck, Y., Hernando, J., Llebaria, A., Fernández-Dueñas, V., Ciruela, F., 2023. *Br. J. Pharmacol.* 180, 958–974. <https://doi.org/10.1111/bph.15645>.
- Manhapra, A., Sullivan, M.D., Ballantyne, J.C., MacLean, R.R., Becker, W.C., 2020. *J. Gen. Intern. Med.* 35, 964–971. <https://doi.org/10.1007/s11606-020-06251-w>.
- McClain, S.P., Ma, X., Johnson, D.A., Johnson, C.A., Layden, A.E., Yung, J.C., Lubejko, S. T., Livrizzi, G., He, X.J., Zhou, J., Chang-Weinberg, J., Ventriglia, E., Rizzo, A., Levinstein, M., Gomez, J.L., Bonaventura, J., Michaelides, M., Banghart, M.R., 2023. *Neuron* 111, 3926–3940.e10. <https://doi.org/10.1016/j.neuron.2023.09.017>.
- Mercadante, S., 2023. *Curr. Treat. Options Oncol.* 24, 1367–1377. <https://doi.org/10.1007/s11864-023-01117-9>.
- Miziev, S., Pawlak, W.A., Howard, N., 2024. *Front. Neurosci.* 17. <https://doi.org/10.3389/fnins.2023.1320441>.
- Mogil, J.S., 2009. *Nat. Rev. Neurosci.* 10, 283–294. <https://doi.org/10.1038/nrn2606>.
- Nadeau, S.E., Wu, J.K., Lawhern, R.A., 2021. *Frontiers in pain research* 2. <https://doi.org/10.3389/fpain.2021.721357>.
- Notartomaso, S., Antenucci, N., Mazzitelli, M., Rovira, X., Boccella, S., Ricciardi, F., Liberatore, F., Gomez-Santacana, X., Imbriglio, T., Cannella, M., Zussy, C., Luongo, L., Maione, S., Goudet, C., Battaglia, G., Llebaria, A., Nicoletti, F., Neugebauer, V., 2024. *Elife* 13. <https://doi.org/10.7554/eLife.94931>.
- Paoletti, P., Ellis-Davies, G.C.R., Mourot, A., 2019. *Nat. Rev. Neurosci.* 20, 514–532. <https://doi.org/10.1038/s41583-019-0197-2>.
- Park, S. II, Brenner, D.S., Shin, G., Morgan, C.D., Copits, B.A., Chung, H.U., Pullen, M.Y., Noh, K.N., Davidson, S., Oh, S.J., Yoon, J., Jang, K.-I., Samineni, V.K., Norman, M., Grajales-Reyes, J.G., Vogt, S.K., Sundaram, S.S., Wilson, K.M., Ha, J.S., Xu, R., Pan, T., Kim, T., Huang, Y., Montana, M.C., Golden, J.P., Bruchas, M.R., Gereau, R. W., Rogers, J.A., 2015. *Nat. Biotechnol.* 33, 1280–1286. <https://doi.org/10.1038/nbt.3415>.
- Rahman, S., Kidwai, A., Rakhimova, E., Elias, M., Caldwell, W., Bergese, S.D., 2023. *Diagnostics* 13, 3689. <https://doi.org/10.3390/diagnostics13243689>.
- Rogers, E., Mehta, S., Shengelia, R., Reid, M.C., 2013. *Clin. Geriatr.* vol. 21.
- Samineni, V.K., Yoon, J., Crawford, K.E., Jeong, Y.R., McKenzie, K.C., Shin, G., Xie, Z., Sundaram, S.S., Li, Y., Yang, M.Y., Kim, J., Wu, D., Xue, Y., Feng, X., Huang, Y., Mickle, A.D., Banks, A., Ha, J.S., Golden, J.P., Rogers, J.A., Gereau, R.W., 2017. *Pain* 158, 2108–2116. <https://doi.org/10.1097/j.pain.0000000000000968>.
- Sanchez-Cano, A., Saldaña-Díaz, J.E., Perdices, L., Pinilla, I., Salgado-Remacha, F.J., Jarabo, S., 2020. *Appl. Opt.* 59, D111. <https://doi.org/10.1364/AO.384614>.
- Stieglitz, T., Gueli, C., Martens, J., Floto, N., Eickenscheidt, M., Sporer, M., Ortmanns, M., 2023. *Microsyst. Nanoeng.* 9, 54. <https://doi.org/10.1038/s41378-023-00527-x>.
- Taura, J., Nolen, E.G., Cabré, G., Hernando, J., Squarzialupi, L., López-Cano, M., Jacobson, K.A., Fernández-Dueñas, V., Ciruela, F., 2018. *J. Contr. Release* 283, 135–142. <https://doi.org/10.1016/j.jconrel.2018.05.033>.
- Vijayvargiya, Priya, Camilleri, M., Vijayvargiya, Pooja, Erwin, P., Murad, M.H., 2020. *Aliment. Pharmacol. Ther.* 52, 37–53. <https://doi.org/10.1111/apt.15791>.
- Volkow, N.D., McLellan, A.T., 2016. *N. Engl. J. Med.* 374, 1253–1263. <https://doi.org/10.1056/NEJMra1507771>.
- Wu, Y., Wu, M., Vázquez-Guardado, A., Kim, J., Zhang, X., Avila, R., Kim, J.-T., Deng, Y., Yu, Y., Melzer, S., Bai, Y., Yoon, H., Meng, L., Zhang, Y., Guo, H., Hong, L., Kanatzidis, E.E., Haney, C.R., Waters, E.A., Banks, A.R., Hu, Z., Lie, F., Chamorro, L. P., Sabatini, B.L., Huang, Y., Kozorovitskiy, Y., Rogers, J.A., 2022. *Nat. Commun.* 13, 5571. <https://doi.org/10.1038/s41467-022-32947-0>.
- Yang, Y., Wu, M., Vázquez-Guardado, A., Wegener, A.J., Grajales-Reyes, J.G., Deng, Y., Wang, T., Avila, R., Moreno, J.A., Minkowicz, S., Dumrongprechachan, V., Lee, J., Zhang, S., Legaria, A.A., Ma, Y., Mehta, S., Franklin, D., Hartman, L., Bai, W., Han, M., Zhao, H., Lu, W., Yu, Y., Sheng, X., Banks, A., Yu, X., Donaldson, Z.R., Gereau, R.W., Good, C.H., Xie, Z., Huang, Y., Kozorovitskiy, Y., Rogers, J.A., 2021. *Nat. Neurosci.* 24, 1035–1045. <https://doi.org/10.1038/s41593-021-00849-x>.
- Yarmolenko, P.S., Moon, E.J., Landon, C., Manzoor, A., Hochman, D.W., Viglianti, B.L., Dewhirst, M.W., 2011. *Int. J. Hyperther.* 27, 320–343. <https://doi.org/10.3109/02656736.2010.534527>.

Zhang, H., Zhao, H., Zhao, X., Xu, C., Franklin, D., Vázquez-Guardado, A., Bai, W., Zhao, J., Li, K., Monti, G., Lu, W., Kobeissi, A., Tian, L., Ning, X., Yu, X., Mehta, S., Chanda, D., Huang, Y., Xu, S., Perez White, B.E., Rogers, J.A., 2021. Adv. Funct. Mater. 31. <https://doi.org/10.1002/adfm.202100576>.

Zhang, Y., Mickle, A.D., Gutruf, P., McIlvried, L.A., Guo, H., Wu, Y., Golden, J.P., Xue, Y., Grajales-Reyes, J.G., Wang, X., Krishnan, S., Xie, Y., Peng, D., Su, C.-J., Zhang, F.,

Reeder, J.T., Vogt, S.K., Huang, Y., Rogers, J.A., Gereau, R.W., 2019. Sci. Adv. 5. <https://doi.org/10.1126/sciadv.aaw5296>.

Zhong, Y., Bellamkonda, R.V., 2007. Brain Res. 1148, 15–27. <https://doi.org/10.1016/j.brainres.2007.02.024>.